

Surface Current Measurements Using X-Band Marine Radar With Vertical Polarization

Weimin Huang, *Senior Member, IEEE*, Ruben Carrasco, Chengxi Shen,
Eric W. Gill, *Senior Member, IEEE*, and Jochen Horstmann

Abstract—In this paper, the retrieval of sea surface current velocity from vertically polarized (V-pol) X-band marine radar data is presented. Three different methods, including the iterative least square approach, the normalized scalar product method, and the polar current shell algorithm, that have been used for horizontally polarized data are employed here. A comprehensive comparison of the performance of the three methods is conducted using the radar images collected by the V-pol radar deployed on the Forschungsplattformen in Nord- und Ostsee No. 3 (FINO3) offshore research platform and the acoustic Doppler current profiler (ADCP) data in the North Sea. The results indicate that all three methods are capable of providing reliable current speed and direction measurements from V-pol data, with similar performance. Based on the experimental data for which the current magnitude is less than 0.5 m/s, the radar-derived results agree best with the ADCP data at a depth of 6–8 m, with the root mean square difference for current velocity x - and y -components being 7.2–8.9 cm/s. The correlation coefficients between the radar-derived and ADCP-measured current velocity components are as high as 0.87–0.93.

Index Terms—Marine radar, remote sensing, surface current, vertical polarization.

I. INTRODUCTION

THE monitoring of ocean waves and currents is of great importance for offshore activities, maritime safety, and coastal protection. Meanwhile, in the broader oceanographic context, such information may facilitate the verification of various wave theories and the understanding of global ocean characteristics. While measurements of waves and currents have been ordinarily performed using *in situ* instruments [e.g., wave buoys and acoustic Doppler current profilers (ADCPs)], a growing interest has been developed in remote sensing technologies using X-band marine radars, which can be more efficient in time and cost and can be employed to make mea-

surements from moving vessels. The X-band radar is well known for its operational flexibility (small dimensions and easy installation) and very high spatial and temporal resolution. For radar backscatter at moderate incidence, the normalized radar cross section (NRCS) is proportional to the spectral density of the surface roughness on scales comparable to the radar wavelength (Bragg scattering). In the case of X-band radar, the radio wavelength is around 3 cm. At grazing incidence, other mechanisms, e.g., scattering from microbreakers, contribute to the NRCS, particularly for horizontal polarization. The radar backscatter is also induced by other scattering mechanisms, e.g., wedge scattering. In general, the long surface waves modulate the small-scale surface roughness that, in turn, modulates the radar backscatter. At grazing incidence, the main modulation mechanisms include tilt and hydrodynamic modulation as well as geometrical shadowing of the radar beam by the waves [1]. These modulation mechanisms lead to the imaging of the surface waves whose wavelengths are greater than twice of the radar resolution. A detailed description of scattering and modulation mechanisms at low grazing incidence can be found in [2]. Since the surface current influences the long waves through the dispersion relation and these waves modulate the wind-generated small-scale roughness that is seen by the radar via Bragg scattering, the current and wave information can be extracted from the radar images.

Since Young *et al.* [3] first described an approach to extract ocean information from a sequence of marine radar images in the 1980s, an increasing number of researchers have been engaged in this field. To date, the real-time measurements of unambiguous directional wave spectra, as well as surface current parameters, have been achieved and commercialized (e.g., the Wave Monitoring System (WaMoS II) developed by the GKSS research center in Germany [4]). The methods of wave inversion from X-band marine radar images can be found in [5]–[11]. Existing current inversion algorithms include the basic least square (LS) fitting technique [3], the weighted LS method [12], the iterative LS (ILS) approach [13], the DiSC method [15], and the normalized scalar product (NSP) procedure [14]. In [16], various modifications have also been proposed and applied to the ILS and NSP algorithms. Most recently, a new strategy to extract the surface current information from X-band marine radar images based on the polar current shell (PCS) has been presented in [17] and [18]. While most traditional current inversion techniques introduced earlier are based on the concept of “correlation” and are performed in Cartesian coordinates, the PCS algorithm involves a sinusoidal curve-fitting process in polar coordinates. Although all the aforementioned current methods have been evaluated using horizontally polarized (H-pol) X-band radar data, very limited research on current derivation

Manuscript received September 16, 2015; revised December 9, 2015 and December 14, 2015; accepted December 15, 2015. The work of W. Huang was supported in part by the Research and Development Corporation Industrial Research and Innovation Fund under Ignite Grant 207765 and in part by the Natural Sciences and Engineering Research Council of Canada (NSERC) under Grant NSERC 402313-2012. The work of E. W. Gill was supported in part by the NSERC under Grant NSERC 238263-2010 and in part by the Atlantic Innovation Fund Award to the Memorial University of Newfoundland.

W. Huang, C. Shen, and E. W. Gill are with the Faculty of Engineering and Applied Science, Memorial University of Newfoundland, St. John's, NL A1B 3X9, Canada (e-mail: weimin@mun.ca; chengxi.shen@mun.ca; ewgill@mun.ca).

R. Carrasco and J. Horstmann are with the Department of Radar Hydrography, Helmholtz-Zentrum Geesthacht Centre for Materials and Coastal Research, 21502 Geesthacht, Germany (e-mail: Ruben.Carrasco@hzg.de; Jochen.Horstmann@hzg.de).

Color versions of one or more of the figures in this paper are available online at <http://ieeexplore.ieee.org>.

Digital Object Identifier 10.1109/TGRS.2015.2509781

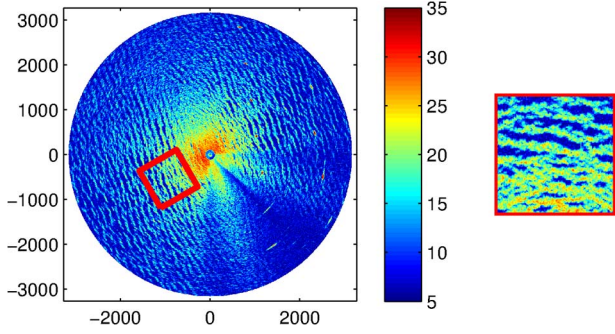


Fig. 1. Example of an X-band marine radar plan position indicator image (left) on which a subimage is indicated by the red box and shown on the right. Color bar indicates backscatter intensity in logarithmic scale.

from vertically polarized (V-pol) X-band marine radar images has been reported. H-pol radar has been widely used for navigation purposes since it minimizes sea clutter and better enables hard target detection [19]. However, a V-pol radar, for which the electric field is in the elevation plane, is superior to H-pol radar in collecting sea clutter. It has been pointed out in [20] that marine radar requires enough sea clutter to obtain satisfactory performance in current and wave information extraction. Thus, V-pol radar may provide better performance in current and wave measurement than H-pol radar, and it has attracted increasing interest. In [21], only the ILS approach was applied to both V-pol and H-pol radar data. Although the LS, ILS, and NSP methods were compared based on both H-pol and V-pol data in [16], only two 30-min V-pol data sets collected under a low sea state were available to compare with two ADCP measurements.

In order to augment the research on ocean mapping using X-band V-pol radar, sea surface currents retrieved from ten days of V-pol X-band nautical radar data are presented in this paper. In addition, a comprehensive comparison of the results obtained using the ILS, NSP, and PCS methods with those from the ADCP is also conducted to show the applicability of these methods to V-pol data collected under varying sea states. Section II briefly introduces the three current algorithms. In Section III, the V-pol radar system and experimental data are detailed, and the current results retrieved from the V-pol data using the three methods are presented and compared. A summary appears in Section IV.

II. CURRENT ALGORITHMS

A typical X-band marine radar image covers an area of 16–64 km². On such a large spatial scale, the illuminated ocean may not be homogeneous, and it may be inappropriate to analyze it as a whole. However, it is reasonable, in many instances, to assume that the areas on a smaller scale (e.g., 1 km²) are homogeneous and that surface current parameters can be resolved at such scales. Thus, prior to applying any current inversion algorithm, a sequence consisting of M rectangular subimages (usually a square each of size $N \times N$ pixels), corresponding to M subareas of the overall region of coverage, must be extracted. An example of the process is illustrated in Fig. 1.

Once the raw subimage sequence $I_0(x, y, t)$ is available, the process of retrieving the current vector $\vec{U}(U, \phi_{\vec{U}})$ for a specific ocean patch may be initiated. Naturally, (x, y) denotes the position on the subimage rather than the full image, and

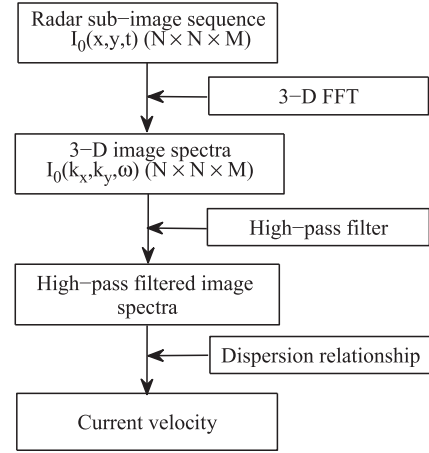


Fig. 2. Block diagram of the current inversion procedure.

t is the time coordinate. In order to determine the surface current speed U and direction $\phi_{\vec{U}}$, the radar subimage sequence is first transformed into the wavenumber–frequency domain using a 3-D fast Fourier transform (3D-FFT) to obtain image spectrum $I_0(k_x, k_y, \omega)$, where k_x and k_y are the wavenumber components in the x - and y -directions, respectively, and ω is the angular frequency of the wave components. All the current retrieval algorithms are based on the wave dispersion relationship, for which the linear (fundamental) mode is given by

$$\omega = \sqrt{gk \tanh(kd)} + \vec{k} \cdot \vec{U} \quad (1)$$

where g is the gravitational acceleration, d is the water depth, and \vec{k} is the wave vector whose magnitude is $k = \sqrt{k_x^2 + k_y^2}$. For deep water, (1) can be simplified as

$$\omega = \sqrt{gk} + \vec{k} \cdot \vec{U} = \zeta(k_x, k_y) + \vec{k} \cdot \vec{U} \quad (2)$$

where $\zeta(k_x, k_y) = \sqrt{gk}$ is the intrinsic frequency of the wave with wavenumber components (k_x, k_y) . According to (2), the current can introduce a Doppler shift that causes the wave energy in the 3-D image spectra to deviate from the ideal (current-free) dispersion shell. By estimating the deviation from the spectral signal, the current velocity can be estimated. The general process of all the current algorithms is depicted in Fig. 2. The difference in these methods usually appears after the image spectra are obtained, and this will be explained in what follows.

A. ILS Approach

The ILS method [13] includes: 1) obtaining an initial current value based on the fundamental mode dispersion relation in (2), for the high-pass-filtered image spectral points whose normalized energy is higher than a threshold of $T_1 = 0.2$, using the LS method [3], and 2) updating results iteratively by classifying the spectral points with normalized energy higher than a lower threshold of $T_2 = 0.02$ into the fundamental and higher harmonic modes as well as aliases. In step (1), the initial values of the east (U_x) and north (U_y) current velocity components are determined as those that minimize the sum-of-squares error function

$$E_1 = \sum_{i=1}^{N_{e1}} [\omega_i - \zeta(k_{x_i}, k_{y_i}) - k_{x_i} U_x - k_{y_i} U_y]^2 \quad (3)$$

where N_{c1} is the number of high-pass-filtered (in the wavenumber–frequency domain) image spectral points with normalized energy higher than T_1 . $\zeta(k_{x_i}, k_{y_i})$ is the calculated ocean wave intrinsic frequency for the selected image spectral points, and k_{x_i}, k_{y_i} and ω_i are the x and y wavenumber components and radian frequency, respectively, of points in the $(k_{x_i}, k_{y_i}, \omega_i)$ space. Since only the fundamental mode wave energy from the spectrum is considered, the number of data points used in (3) may not be large enough to provide a robust result. Moreover, when the sampling rate is low or the current speed of encounter (combination of the velocities of radar platform and current) is high, aliasing may occur. Thus, the initially calculated current result may not be suitably precise, and refinement is required.

In step (2), a lower energy threshold of T_2 is used to increase the number of spectral points involved in the LS calculation to N_{c2} . Both the fundamental and higher order harmonic wave components are considered with the frequency of the p th harmonic being given by

$$\omega_p = \pm(p+1)\sqrt{\frac{gk}{p+1}} + \vec{k} \cdot \vec{U}', \quad p (p = 0, 1, 2, \dots). \quad (4)$$

Of course, $p = 0$ is indicative of the fundamental. In (4), the initial value of the current velocity \vec{U}' is obtained from (3). ω_p is used to determine the harmonic modes and to eliminate the aliasing effect for a given spectral point using the properties of periodicity and point symmetry about the origin, as explained in [13]. As a result, the angular frequency of the spectral point may be corrected to $S_p(k_{x_i}, k_{y_i})$, and a new current velocity can be found by minimizing

$$E_2 = \sum_{i=1}^{N_{c2}} [\omega_i - S_p(k_{x_i}, k_{y_i}) - k_{x_i}U_x - k_{y_i}U_y]^2. \quad (5)$$

This new current velocity is used as \vec{U}' in (4), and the process is repeated a number of times (typically about ten) to obtain a final acceptable result.

B. NSP Method

The NSP method [14] determines the current velocity as the value that maximizes the NSP

$$V(\vec{U}) = \frac{\langle |I_1(k_x, k_y, \omega)|, G(k_x, k_y, \omega, U_x, U_y) \rangle}{\sqrt{P_I P_G}}. \quad (6)$$

In (6), $I_1(k_x, k_y, \omega)$ is the high-pass-filtered (in the wavenumber–frequency domain) image spectrum; P_I and P_G are the power of $I_1(\cdot)$ and $G(\cdot)$, respectively; and $G(\cdot)$ is the characteristic function defined as

$$G(\vec{k}, \omega, \vec{U}) = \begin{cases} 1, & \text{if } \left| \sqrt{gk} + \vec{k} \cdot \vec{U} - \omega(\vec{k}) \right| \leq \frac{\Delta\omega}{2} \\ 0, & \text{otherwise} \end{cases} \quad (7)$$

in which $\Delta\omega$ is the angular frequency resolution. Although only the fundamental components are used in the NSP method, the aliased parts are filtered out by the characteristic function G [14]. Unlike the ILS approach, the NSP method does not require the step of choosing an optimal threshold for the image spectra. Similar to the ILS algorithm, the NSP method has been shown

to be applicable to radar data collected on a moving vessel [14]. It should be mentioned that the retrieved so-called current velocity from shipborne radar data is the velocity of encounter between the ship (moving or not moving) and the waves. For such a case, the ship velocity over ground must be known, in order to estimate that of the surface current. In order to reduce the computational cost associated with seeking the optimal current velocity within a reasonable range for both U_x and U_y , the scheme using variable search ranges and resolutions proposed in [16] is incorporated into the NSP method for the analysis here.

C. PCS Algorithm

The PCS algorithm that was introduced in [17] and [18] includes the following four major steps.

1) *3D-FFT*: While this step appears in virtually all existing current inversion algorithms, there are still two things that must be clarified in this context. First, before performing the 3D-FFT, the subimage sequence is multiplied by a smooth tapering function $W(n)$ [22] to mitigate the Gibbs phenomenon in both spatial and temporal domains. Moreover, in order to reduce the noise level and obtain a smoother image spectrum, the 3D-FFT involves $256 \times 256 \times 256$ points with zero padding being used beyond the original data size of $N \times N \times M$. At a slight cost of computing time, this move allows more data points to enter the later curve-fitting process, which in return significantly improves the performance of the algorithm.

2) *Extraction of the Dispersion Shell*: The next step is to extract the dispersion shell based on the fundamental mode wave dispersion relationship in (2) from the high-pass-filtered 3-D image spectrum $I_1(k_x, k_y, \omega)$. Equation (2) indicates that, for each pair of (k_{xi}, k_{yi}) , $i = 1, 2, \dots, 256$, only one spectral point with a frequency of ω_j will be located on the dispersion shell, and this is associated with an ocean wave component. This ω_j for a specific pair (k_{xi}, k_{yi}) is determined as the frequency of the peak image spectral point among all the points with the wavenumber pair being (k_{xi}, k_{yi}) [17]. If the energy of the spectral peak for (k_{xi}, k_{yi}) is lower than a threshold ($= I_1(k_x, k_y, \omega)|_{\max}/2000$ here), all data points with wavenumber pair being (k_{xi}, k_{yi}) are excluded from further processing. This procedure may eliminate possible interference from low-energy background noise spikes and can also reduce the number of iterations for subsequent steps. In addition, if only one prominent peak for (k_{xi}, k_{yi}) is detected (the criterion here being that no other peak reaches one-third of the energy of the main peak), the corresponding ω is extracted as ω_j ; otherwise, ω_j is set to zero. After repeating this procedure for each (k_{xi}, k_{yi}) pair, a coarse dispersion shell $\omega_0(k_x, k_y)$ can be constructed from all the identified peak points with nonzero ω_j .

3) *Transformation to the PCS*: According to the dispersion relation described in (2), it should be noted that the $\omega_0(k_x, k_y)$ obtained by the procedure mentioned in Section II-C2 actually consists of two portions from different sources. The first term for deep-water waves, i.e., \sqrt{gk} in (2), arises from ocean wave components, while the second term, i.e., $\vec{k} \cdot \vec{U}$, comes from the near-surface current effects. Using $\bar{\theta}$ to denote the intersection angle between the current direction and the wave vector, i.e., $\bar{\theta} = |\theta_{\vec{k}} - \phi_{\vec{U}}|$, (2) may be rewritten as

$$\omega_U(k_x, k_y) = \vec{k} \cdot \vec{U} = kU \cos \bar{\theta} = \omega_0(k_x, k_y) - \sqrt{gk} \quad (8)$$

where $\omega_U(k_x, k_y)$ represents the frequency shift induced by surface current and is thus referred to as the “current shell” in Cartesian coordinates (i.e., Cartesian current shell). In order to better examine this current shell to reveal the hidden current parameters U and ϕ_U , we next transform the Cartesian shell into polar coordinates (referred to as the PCS). The resulting PCS is denoted by $\omega_U(k, \theta_k)$. This allows inspection of the data points along a specific radius or direction, where either θ_k (i.e., $\bar{\theta}$) or U is fixed, so that the unknowns may be dealt with one at a time. For reasonable accuracy, the polar shell should have at least a size of 128×360 , i.e., 128 points in the radial direction and 360 angular elements.

4) *Determination of Current Parameters:* The next step is to detect any outliers along each radial direction of $\omega_U(k, \theta_k)$. The outliers refer to the interfering spectral points due to noise that fall in the PCS. The interference may severely affect the later LS fit and, thus, must be removed. According to (8), for a particular radial direction in the wavenumber plane, the intersection angle $\bar{\theta}$ is fixed, so that ω_U/k should remain constant. Thus, Grubbs’ test [23] is used to detect one outlier at a time, and this outlier is removed and the test is repeated until no outliers are detected [17]. It should be noted that all the points corresponding to $\omega_0(k_x, k_y) = 0$ should be removed from the vector $[(\omega_{U1}/k_1)(\omega_{U2}/k_2) \dots (\omega_{U128}/k_{128})]$, for each radial direction in the polar shell plane, before Grubbs’ test.

Having eliminated the interference in all radial directions, LS curve fitting along each circumferential direction (i.e., for each definite radius) is implemented using the model function $f(U, \bar{\theta}) = \omega_U/k = U \cos \bar{\theta} = U \cos |\theta_k - \phi_U|$. It should be noted that, if the number of surviving points within a circumferential vector is smaller than 10, the fitting process should be aborted for this radius. The angle corresponding to the maximum of the estimated function $f(U, \bar{\theta})$ is determined to be the current direction, and the amplitude of this sinusoidal function is the current speed. The results may be averaged over a band of varying radius to generate an accurate current velocity.

III. EXPERIMENTAL RESULTS

A. Radar System and Data Overview

A V-pol nautical X-band radar with power of 12 kW was deployed on the offshore Forschungsplattformen in Nord- und Ostsee No. 3 (FINO3) research platform in the North Sea, in 2014. The FINO3 platform, which is located at $55^\circ 11.7' \text{ N}$, $7^\circ 9.5' \text{ E}$, is about 80 km west of the island of Sylt in Germany. About ten days of radar data were collected in late July and August. The antenna, which was mounted 45 m above the water, scanned the sea surface with a rotation speed of approximately 28 r/min, an azimuthal resolution of about 1° , and a range resolution of 7.5 m. The water depth in the radar coverage area is 28 m, and this may be roughly treated as deep water, since the typical observed peak wavelength was about 56 m, although it generally varied from 25 to 156 m during the experiment period. One radar sequence of 128 images (about 4.5 min long) was collected every half an hour. The subimages that were selected from the up-wave direction for current retrieval are of size 128×128 pixels. The up-wave direction was retrieved from the radar-derived wave spectra using the method in [5], and the value was updated for every subimage sequence. The center of the subarea is about 630 m from the platform.

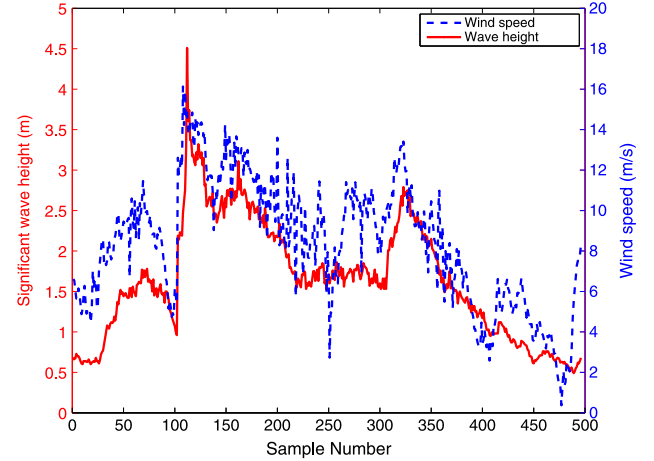


Fig. 3. Significant wave height (blue dash) and wind speed (red solid) time sequence.

The platform is stationary and will not cause motion-induced effects on the current measurements, and there is no blockage introduced by the platform in the direction of the subarea. The ILS approach developed by the Helmholtz-Zentrum Geesthacht Centre for Materials and Coastal Research, the NSP method, and the PCS algorithm all use a sequence of 128 images to produce one result. In order to validate the radar-derived current results, the data of a bottom-mounted ADCP that is located 100 m south of the FINO3 platform were used as ground truth. The ADCP data showed that the current speed in the area was up to 0.5 m/s, and clear tidal signals were evident in the record.

B. Current Retrieval Results and Discussion

In [20], it was pointed out that the H-pol X-band radar requires the sea surface wind to be higher than 3 m/s to generate enough roughness to achieve a good performance in current and wave mapping. Under a low sea state, the signal-to-noise ratio (SNR) of the radar images tends to be low, and the reliability of the inversion process may be adversely affected. As in [7], the SNR values shown in the subsequent part of this paper were calculated from the spectrum using a wave dispersion filter. In order to evaluate the effect of sea state on current retrieval results from the V-pol data, the buoy-measured significant wave heights and anemometer-recorded wind speeds for the experimental period are shown in Fig. 3. The wind data were acquired by an anemometer installed at a 30-m height above sea level, and a 10-min averaging process was used. The wave height was measured by a Datawell Waverider buoy, which was less than 1 km away from the Fino3 platform. Fig. 4 illustrates the comparison of the ADCP-measured (at 8-m depth) and radar-derived current speed and direction for the whole data set. A portion (around two days in length) of Fig. 4 was zoomed in and displayed in Fig. 5, from which a tidal signal with a period of 12 h can be clearly seen. In Fig. 4, outliers were observed in the later portion of the results obtained using the three current algorithms shown in these figures. By referring to Fig. 3, it can be observed that the sea state associated with these outliers was low, with a significant wave height of about 0.6 m and a wind speed lower than 2 m/s. It should be noted that radar-derived current speed and direction using the PCS algorithm were set as zeros (outliers) when the number of data points qualifying for curve fitting was lower than the predefined threshold. These

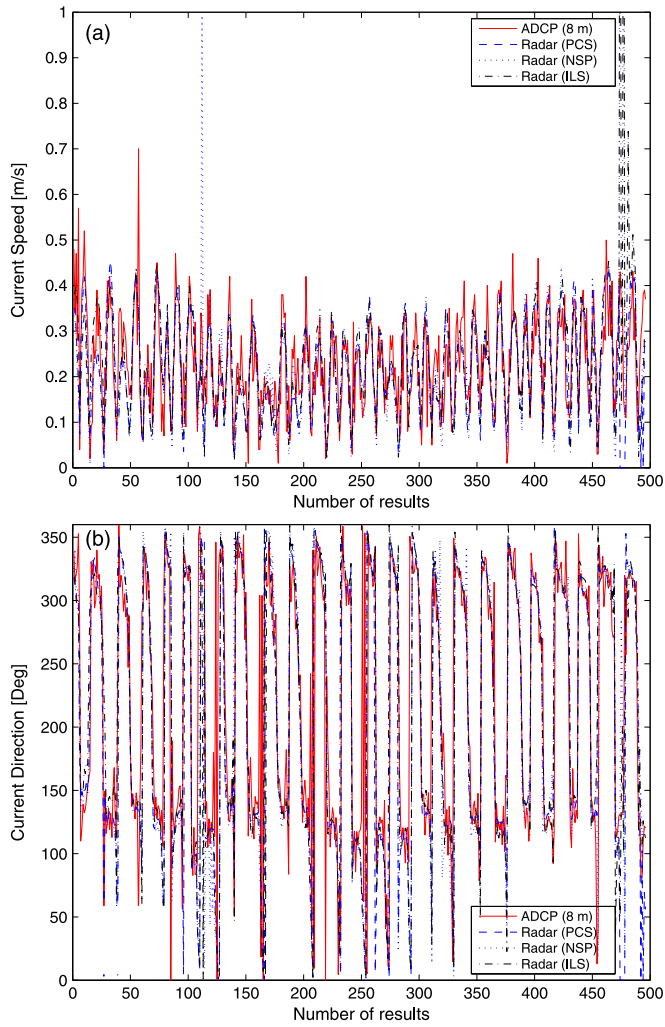


Fig. 4. Comparison of ADCP-measured (at 8-m depth) and radar-derived current (a) speed and (b) direction.

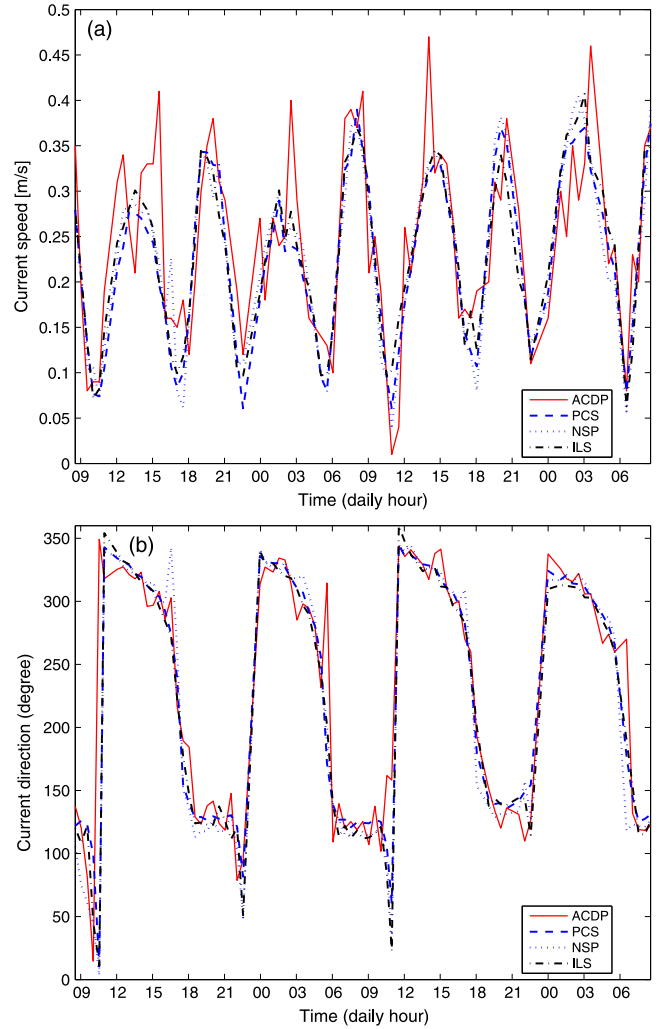


Fig. 5. Zoomed comparison of ADCP-measured (at 8-m depth) and radar-derived current (a) speed and (b) direction for a period of around two days.

corresponding points were also treated as outliers in the NSP results. For the ILS approach, the current results derived from radar data with SNR lower than 4 dB were regarded as outliers. Based on this criterion, there are only 8 outliers for ILS and 6 for NSP and PCS in 494 data points. In other words, the number of data points remaining after quality control is 486, 488, and 488 for ILS, NSP, and PCS, respectively.

Excluding the outliers, the scatter plots for current speed and direction derived using the three algorithms are displayed in Fig. 6, along with the corresponding significant wave heights. It can be concluded that all three methods are able to provide good measurements of current velocity, and the correlation coefficients between the radar and ADCP values are 0.70–0.75 and 0.76–0.83 for speed and direction, respectively. The RMS differences of the radar-derived current speeds using the ILS, NSP, and PCS methods are 7.5, 8.0, and 7.3 cm/s, respectively. The corresponding RMS difference of current direction is less than 35° , for all three methods. Since the current speed is lower than 0.5 m/s, it is not appropriate to investigate the error only in terms of speed and direction. When the current magnitude is small, a small error in either the north or east component of the current may lead to a very large error in direction estimation. Here, the comparison and error analysis are conducted in terms

of current velocity components. Excluding the outliers, the scatter plots for the respective differences in the east (x) and north (y) components of the current vector measured by the ADCP and radar are displayed in Fig. 7, along with the corresponding significant wave heights. It is shown in Fig. 7 that the scatter plots of all three methods look more or less the same. The radar-derived current velocities were also compared with those measured by the ADCP at the depths of 4, 6, and 12 m. The bias, RMS difference, and correlation coefficient of the results with outliers removed are summarized in Table I. Based on the V-pol data used here, it is observed that the radar-derived current velocity components using these three methods agree best with the ADCP measurements at a depth of 6 m, by observing bias, but the results agree best with the ADCP data at the 8-m depth, in terms of RMS difference and correlation coefficient. It should be noted, as discussed as a general principle in [24], that the radar-derived current result is a weighted average over a water depth on the order of $\lambda/(4\pi)$, where λ is the wavelength of the ocean waves visualized by the radar. This rule of thumb applies only if the current profile is assumed to be logarithmic with depth. However, as explained in [25], for the case of marine radar, it is not possible to determine precisely what value to use for the effective depth associated with the measured current.

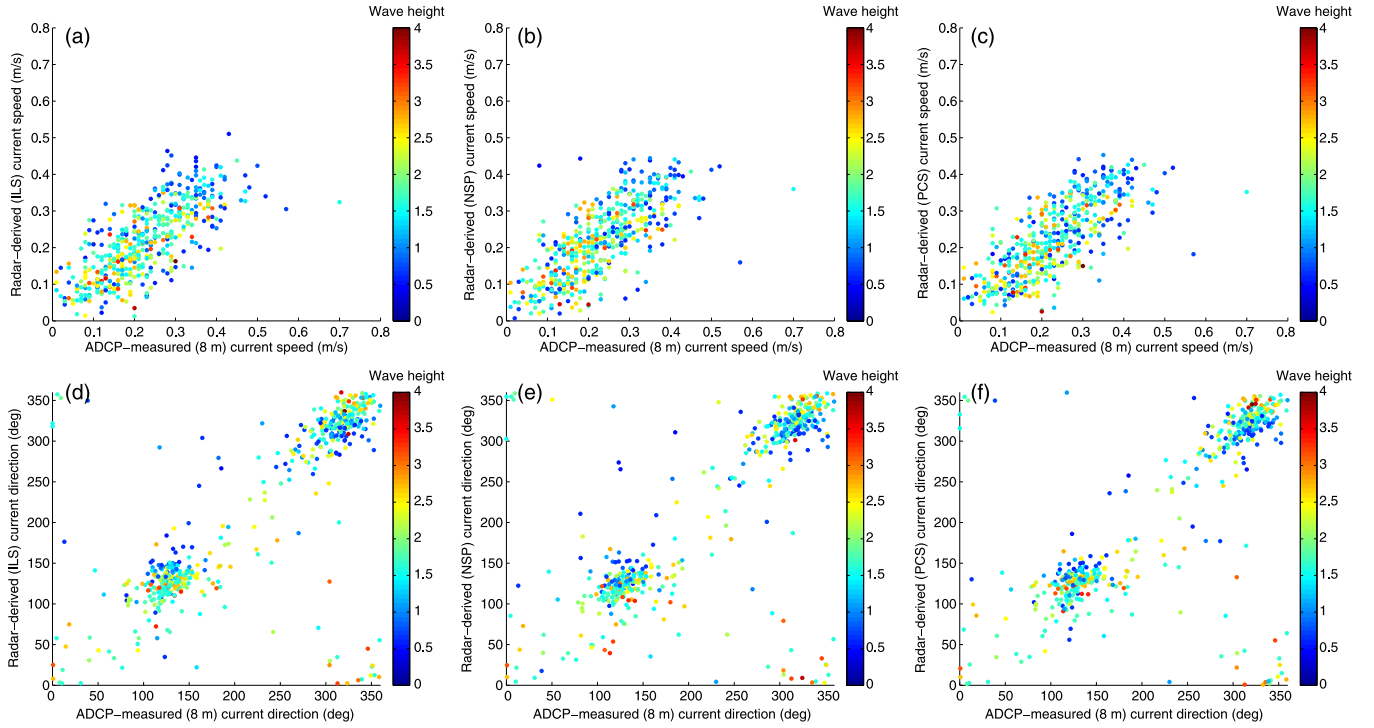


Fig. 6. Comparison of current (a)–(c) speed and (d)–(f) direction measured by ADCP (at 8-m depth) and radar using the (a) and (d) ILS approach; (b) and (e) NSP method; (c) and (f) PCS algorithm.

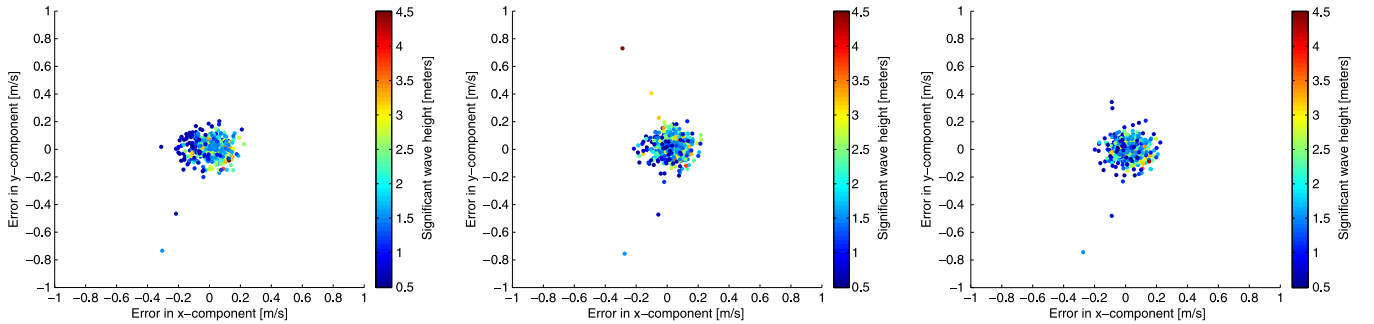


Fig. 7. Scatter plot of the difference of current vector east (x) and north (y) components measured by ADCP (at 8-m depth) and radar. (Left) ILS; (middle) NSP; (right) PCS.

TABLE I
STATISTICS OF BIAS, RMS DIFFERENCE, AND CORRELATION COEFFICIENT OF CURRENT VELOCITY COMPONENTS

Depth (m)	Algorithm	x -component			y -component		
		bias (cm/s)	RMS difference (cm/s)	correlation coefficient	bias (cm/s)	RMS difference (cm/s)	correlation coefficient
4 m	ILS	-2.98	9.05	0.87	4.46	9.70	0.86
	NSP	-1.59	9.00	0.87	5.38	11.39	0.81
	PCS	-1.16	8.48	0.88	3.53	9.02	0.87
6 m	ILS	1.20	8.16	0.90	0.65	7.25	0.91
	NSP	2.66	7.72	0.92	1.53	8.39	0.89
	PCS	3.10	7.60	0.93	-0.31	7.23	0.91
8 m	ILS	0.80	8.29	0.89	0.57	7.69	0.90
	NSP	2.27	7.74	0.91	1.48	8.86	0.87
	PCS	2.71	7.73	0.92	-0.37	7.87	0.90
12 m	ILS	2.38	9.80	0.86	1.06	9.68	0.83
	NSP	3.85	9.96	0.87	1.92	10.47	0.80
	PCS	4.28	10.11	0.87	0.08	9.40	0.83

It may also be pointed out that the ADCP measurement close to the surface may not have good quality because the strong

echo from the surface can overwhelm the sidelobe suppression of the ADCP transducer [26]. Since the differences between

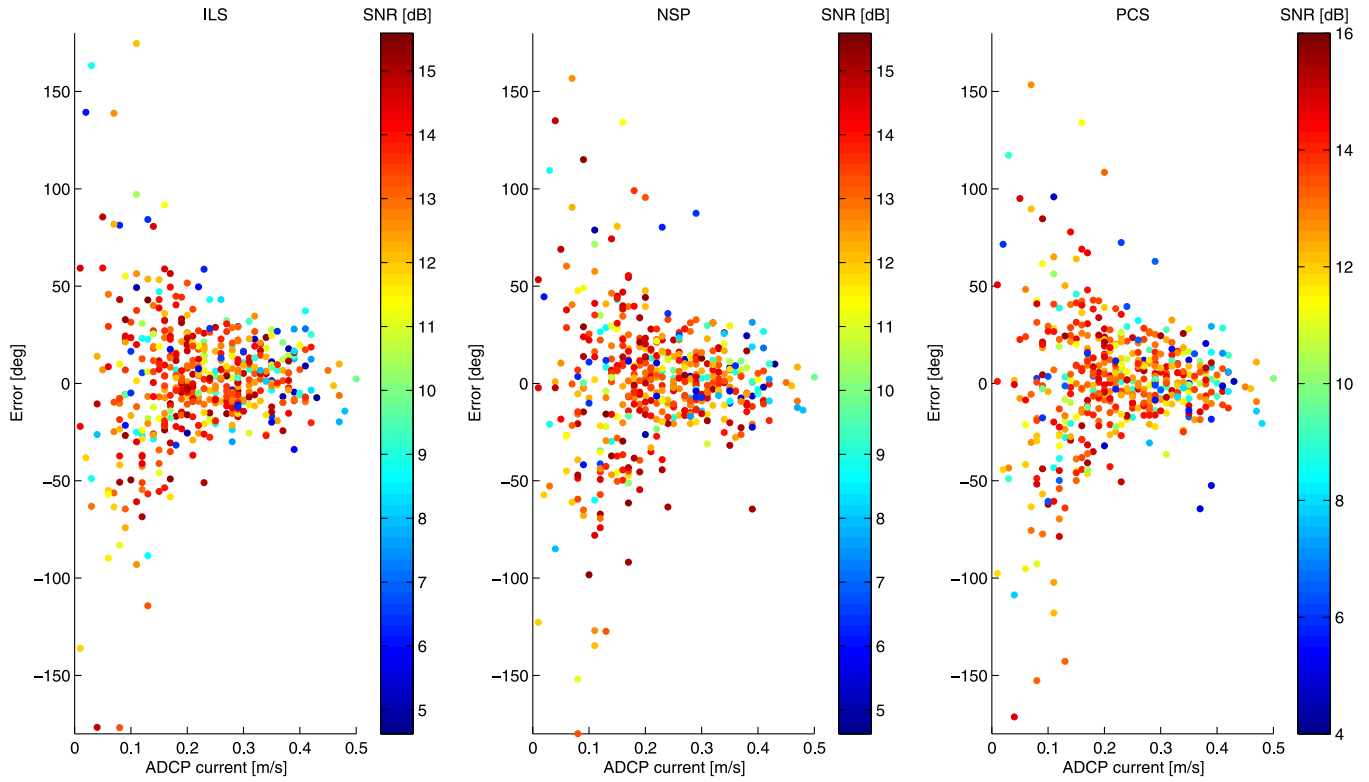


Fig. 8. Distribution of current direction estimation error with respect to ADCP-measured current speed. (Left) ILS; (middle) NSP; (right) PCS.

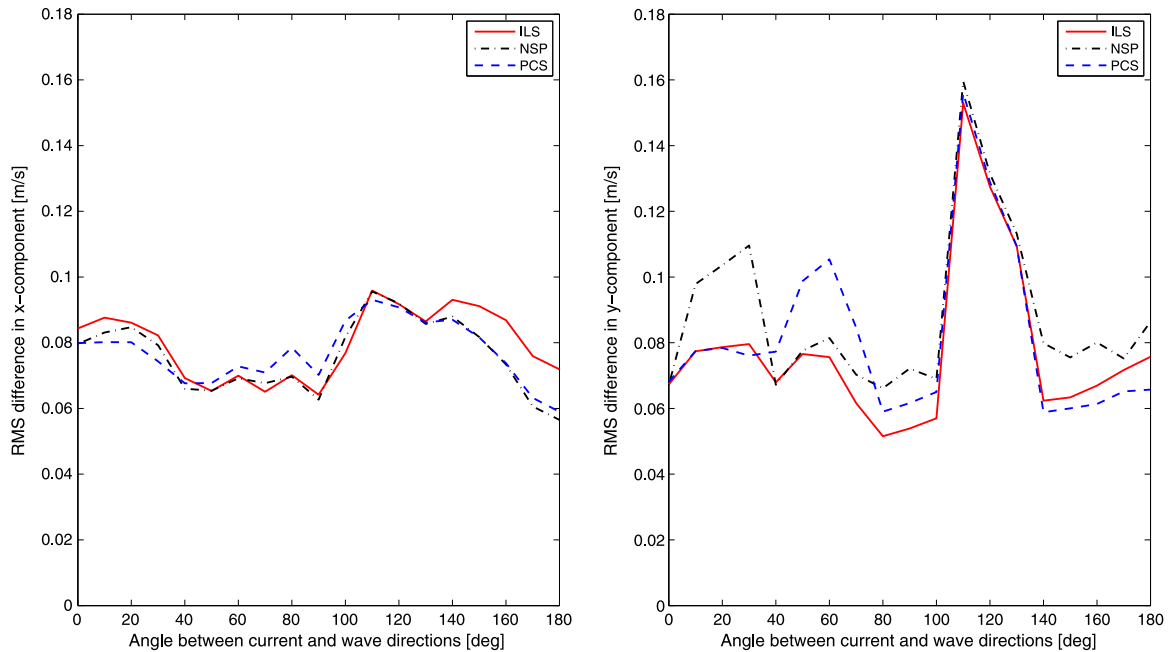


Fig. 9. Dependence of radar-derived current speed RMS difference on the angle between wave and current directions. (Left) x -component; (right) y -component.

the radar-measured and ADCP-recorded current speeds are so similar for the 6- and 8-m depths, the ADCP data from the 8-m depth is used for further detailed comparison. By comparing the radar results with those of ADCP collected at the depth of 8 m, the RMS difference of the radar-derived current velocity components using the ILS, NSP, and PCS methods are 7.69–8.29, 7.74–8.86, and 7.73–7.87 cm/s, respectively. It can be concluded that all three methods can provide good measurements of current velocity components with an RMS

difference between the radar and ADCP values of 7–9 cm/s. In addition, the correlation coefficients between the ADCP-measured current velocity components and radar-derived results using the three methods are comparable as 0.87–0.93. The current direction estimation error depends on the magnitude of the current speed. The distribution of errors in retrieved current direction with respect to ADCP-measured current speed is illustrated in Fig. 8. It can be clearly seen that the estimation error decreases as current speed increases. It should be noted that the

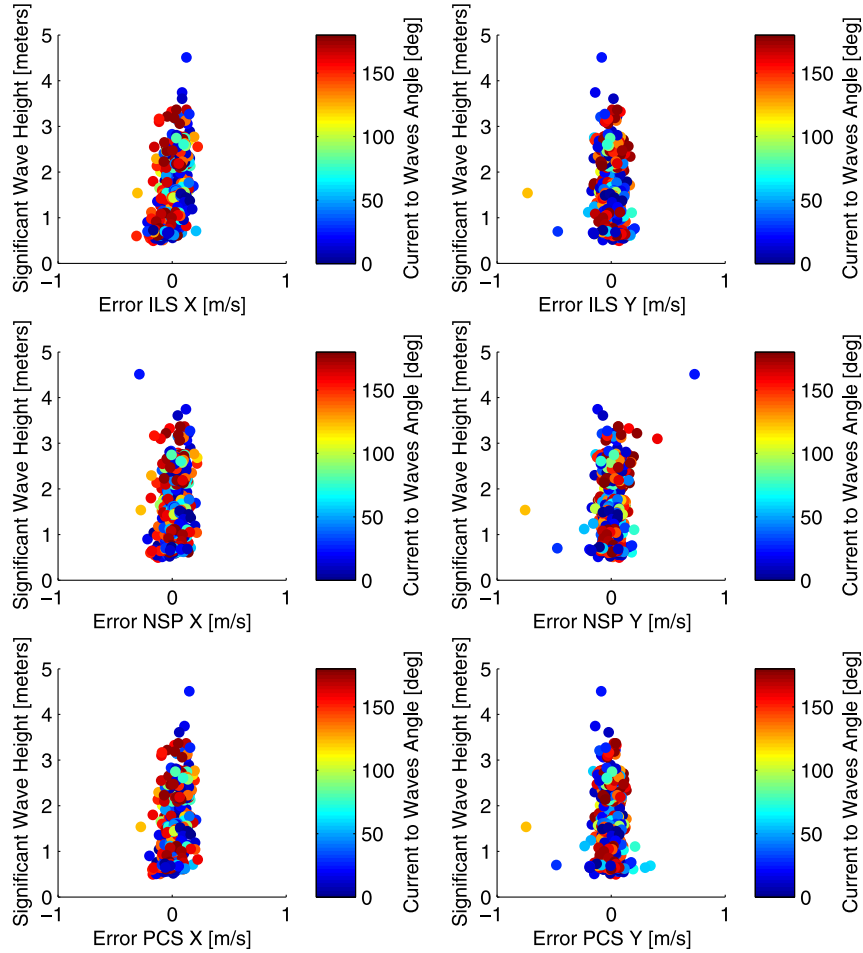


Fig. 10. Dependence of current velocity component measurement error on significant wave height. (Top left) x -component (ILS); (top right) y -component (ILS); (middle left) x -component (NSP); (middle right) y -component (NSP); (bottom left) x -component (PCS); (bottom right) y -component (PCS).

radar-derived current results represent spatial average values within the subarea, whereas the ADCP data represent point measurements at the deployment location. This may account for some of the differences between the radar and ADCP results. However, these results show that all three current algorithms are able to provide good estimates, as compared to the ADCP.

The dependence of the current velocity component RMS differences on the angle between the current direction and the dominant wave direction is depicted in Fig. 9, from which the performances of the three methods are also found to be close to each other. It can also be observed that the RMS difference for both x - and y -components is maximum, when the current direction is perpendicular to the dominant wave direction, and it is 0.05–0.1 m/s, when the current is not perpendicular to the dominant wave direction. From (2), it can be inferred that current with any speed will generate a zero Doppler shift, if the current direction is perpendicular to the dominant wave direction. For such a case, the component of the current can only be estimated due to the directional spread of the wave field. Thus, the estimation error may increase when the current direction is perpendicular. However, the situation may improve for an area with a multimodal wave field, if the direction of one of the modes is not perpendicular to the current.

Investigation of the dependence of current velocity component measurement error on wind speed, significant wave height, and peak wave period was also conducted. Because the North

Sea is usually dominated by wind sea, the wind speed and the significant wave height are not independent of each other. The wind speed sets a lower limit to the methods. No obvious dependence of estimation error on wind speed and peak wave period can be observed. The dependence of error on significant wave height is illustrated in Fig. 10. It is clearly shown in Fig. 10 that better current velocity results are obtained under sea states with higher significant wave height.

IV. CONCLUSION

An analysis of current information retrieved from V-pol X-band marine radar images has been presented. Three current algorithms (ILS, NSP, and PCS) were applied to the V-pol radar data. The comparison of the radar-derived results with ADCP data of different depths showed that all three methods are able to provide current estimates similar to those obtained from the ADCP. It was found that the current results derived from the V-pol radar agreed best with ADCP data collected at a depth of 6–8 m. For these depths, the RMS difference in the current velocity components between the radar and ADCP is 7.2–8.9 cm/s. The correlation between the radar-derived and ADCP-measured results is high, with a correlation coefficient of 0.87–0.93. All three methods exhibit similar performance. This implies that the technology of current measurement using X-band marine radar has become sufficiently mature and the

emphasis perhaps may be legitimately shifted from research methodology toward applications. The analysis also validated that V-pol radar is able to measure sea surface current velocities with very few outliers.

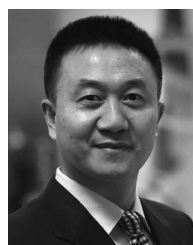
The comparison analysis here was conducted based only on V-pol radar data collected on a stationary platform. Further validation using data from a moving vessel is required. When the radar is on a moving ship, the ship velocity has to be known in order to estimate the actual current velocity. Aliasing will occur for shipborne radar data when the ship speed is high. It should be pointed out that only the ILS approach involves dealiasing to reconstruct the dispersion shells for current calculation. On the other hand, for the NSP method, the aliased parts are eliminated from the current determination by the characteristic function [14], and for the PCS algorithm, this is accomplished by Grubbs' test [17]. Thus, in these latter two cases, aliasing has negligible effect on the current estimation. Furthermore, comparison of the current retrieval using H-pol and V-pol radar is worth pursuing.

ACKNOWLEDGMENT

The authors would like to thank Dr. J. Seemann at the Helmholtz-Zentrum Geesthacht in Germany, for his time and input to help improve the manuscript, and the Bundesamt fuer Seeschifffahrt und Hydrographie (BSH), for the provision of the ADCP data.

REFERENCES

- [1] L. B. Wetzel, "Electromagnetic scattering from the sea at low grazing angles," in *Surface Waves and Fluxes*. Dordrecht, The Netherlands: Kluwer, pp. 109–171.
- [2] G. S. Brown, "Special issue on low-grazing-angle backscatter from rough surfaces," *IEEE Trans. Antennas Propag.*, vol. 46, no. 1, pp. 1–2, Jan. 1998.
- [3] I. R. Young, W. Rosenthal, and F. Ziemer, "Three-dimensional analysis of marine radar images for the determination of ocean wave directionality and surface currents," *J. Geophys. Res.*, vol. 90, no. C1, pp. 681–682, Jan. 1985.
- [4] F. Ziemer, "An instrument for the survey of the directionality of the ocean wave field," in *Proc. WMO/IOC Workshop Oper. Ocean Monit. Surf. Based Radars*, Geneva, Switzerland, Mar. 1995, vol. 32, pp. 81–87.
- [5] J. C. Nieto-Borge, K. Reichert, and J. Dittmer, "Use of nautical radar as a wave monitoring instrument," *Coastal Eng.*, vol. 3/4, pp. 331–342, Aug. 1999.
- [6] J. C. Nieto-Borge, R. G. Rodriguez, K. Hessner, and I. P. Gonzales, "Inversion of marine radar images for surface wave analysis," *J. Atmos. Ocean. Technol.*, vol. 21, no. 8, pp. 1291–1300, Aug. 2004.
- [7] J. C. Nieto-Borge, K. Hessner, P. Jarabo-Amores, and D. de la Mata-Moya, "Signal-to-noise ratio analysis to estimate ocean wave heights from X-band marine radar image time series," *IET Radar Sonar Navig.*, vol. 2, no. 1, pp. 35–41, Feb. 2008.
- [8] R. Gangekar, "An algorithm for estimation of wave height from shadowing in X-band radar sea surface images," *IEEE Trans. Geosci. Remote Sens.*, vol. 52, no. 6, pp. 3373–3381, Jun. 2014.
- [9] Z. Chen, Y. He, B. Zhang, Z. Qiu, and B. Yin, "A new algorithm to retrieve wave parameters from marine X-band radar image sequences," *IEEE Trans. Geosci. Remote Sens.*, vol. 52, no. 7, pp. 4083–4091, Jul. 2014.
- [10] W. Huang, E. W. Gill, and J. An, "Iterative least-squares-based wave measurement using X-band nautical radar," *IET Radar Sonar Navig.*, vol. 8, no. 8, pp. 853–863, Oct. 2014.
- [11] J. An, W. Huang, and E. W. Gill, "A self-adaptive wavelet-based algorithm for wave measurement using nautical radar," *IEEE Trans. Geosci. Remote Sens.*, vol. 53, no. 1, pp. 567–577, Jan. 2015.
- [12] R. Gangekar, "Ocean current estimated from X-band radar sea surface images," *IEEE Trans. Geosci. Remote Sens.*, vol. 40, no. 4, pp. 783–792, Apr. 2002.
- [13] C. M. Senet, J. Seemann, and F. Ziemer, "The near-surface current velocity determined from image sequences of the sea surface," *IEEE Trans. Geosci. Remote Sens.*, vol. 39, no. 3, pp. 492–505, Mar. 2001.
- [14] F. Serafino, C. Lugni, and F. Soldovieri, "A novel strategy for the surface current determination from marine X-band radar data," *IEEE Geosci. Remote Sens. Lett.*, vol. 7, no. 2, pp. 231–235, Apr. 2010.
- [15] C. M. Senet, J. Seemann, S. Flampouris, and F. Ziemer, "Determination of bathymetric and current maps by the method DiSC based on the analysis of nautical X-band radar image sequences of the sea surface," *IEEE Trans. Geosci. Remote Sens.*, vol. 46, no. 8, pp. 2267–2279, Aug. 2007.
- [16] W. Huang and E. Gill, "Surface current measurement under low sea state using dual polarized X-band nautical radar," *IEEE J. Sel. Topics Appl. Earth Observ. Remote Sens.*, vol. 5, no. 6, pp. 1868–1873, Dec. 2012.
- [17] C. Shen, W. Huang, and E. Gill, "An alternative method for surface current extraction from X-band marine radar images," in *Proc. IEEE IGARSS*, Quebec, QC, Canada, Jul. 2014, pp. 4370–4373.
- [18] C. Shen, W. Huang, E. Gill, R. Carrasco, and J. Horstmann, "An algorithm for surface current retrieval from X-band marine radar images," *Remote Sens.*, vol. 7, no. 6, pp. 7753–7767, Jun. 2015.
- [19] J. N. Briggs, *Target Detection by Marine Radar*. London, U.K.: The Institution of Electrical Engineers, 2004.
- [20] J. C. Nieto-Borge and C. Guedes-Soares, "Analysis of directional wave fields using X-band navigation radar," *Coastal Eng.*, vol. 40, no. 4, pp. 375–391, Jul. 2000.
- [21] L. Cui, Y. He, H. Shen, and H. Lu, "Measurements of ocean wave and current field using dual polarized X-band radar," *Chin. J. Oceanol. Limnol.*, vol. 28, no. 5, pp. 1021–1028, Sep. 2010.
- [22] J. W. Tukey, "An introduction to the calculations of numerical spectrum analysis," in *Spectral Analysis of Time Series*. New York, NY, USA: Wiley, 1967, pp. 25–46.
- [23] F. E. Grubbs, "Procedures for detecting outlying observations in samples," *Technometrics*, vol. 11, no. 1, pp. 1–10, Feb. 1969.
- [24] R. H. Stewart and J. W. Joy, "High radio measurements of surface current," *Deep-Sea Res.*, vol. 21, no. 12, pp. 1039–1049, Dec. 2014.
- [25] B. Lund, H. C. Graber, J. Campana, and E. Terrill, "Near-surface current shear measured by marine radar," in *Proc. IEEE/OES 11th Current, Waves Turbulence Meas. Workshop*, St. Petersburg, FL, USA, Mar. 2015, pp. 1–6.
- [26] Acoustic Doppler Current Profiler Principles of Operation: A Practical Primer, Jan. 2011. [Online]. Available: <http://www.rdiinstruments.com>



Weimin Huang (M'10–SM'13) received the B.S., M.S., and Ph.D. degrees from Wuhan University, Wuhan, China, in 1995, 1997, and 2001, respectively, all in radio physics. He also received the M.Eng. degree from the Memorial University of Newfoundland, St. John's, NL, Canada.

From 2008 to 2010, he was a Design Engineer with Rutter Technologies. Since 2010, he has been with the Faculty of Engineering and Applied Science, Memorial University of Newfoundland, where he is currently an Associate Professor. His past and

present research involves the mapping of oceanic surface parameters via high-frequency ground wave radar, X-band marine radar and, more recently, global navigation satellite systems.

Dr. Huang was a recipient of a Postdoctoral Fellowship in engineering electromagnetics from the Memorial University of Newfoundland.



Ruben Carrasco received the M.S. degree in industrial engineering from the Universidad de Alcalá, Madrid, Spain, in 2009.

Since 2004, he has been with Lectra, Madrid, as a Computer-Aided-Design and Computer-Aided-Manufacturing Expert. Between 2008 and 2009, he was with the Department of Signal Theory and Communications, Universidad de Alcalá, working on his M.S. thesis related to ship detection in marine environments. He is a Research Engineer with the Department of Radar Hydrography, Institute of

Coastal Research, Helmholtz-Zentrum Geesthacht Centre for Materials and Coastal Research, Geesthacht, Germany. His research interests include artificial intelligence systems, radar signal processing, and pattern recognition.



Chengxi Shen received the B.Sc. degree in electronic science and technology from Wuhan University, Wuhan, China, in 2008 and the M.Eng. degree in electrical engineering from the Memorial University of Newfoundland, St. John's, NL, Canada, in 2013.

He is currently with the Faculty of Engineering and Applied Science, Memorial University of Newfoundland. His research interest involves the development of the high-frequency radar cross-section model and the maritime navigation radar current algorithm.



Eric W. Gill (M'00–SM'05) received the B.Sc. degree in physics and the M.Eng. and Ph.D. degrees in electrical engineering from the Memorial University of Newfoundland, St. John's, NL, Canada, in 1977, 1990, and 1999, respectively.

In 1977, he was a Lecturer in physics with the College of the North Atlantic (formerly, Cabot Institute of Applied Arts and Technology), St. John's, NL, Canada. Since 2000, he has been with the Faculty of Engineering and Applied Science, Memorial University of Newfoundland, where he is currently

a Professor carrying out teaching and research in theoretical and applied electromagnetics. His special interest lies in the scattering of high-frequency electromagnetic radiation from time-varying randomly rough surfaces, with particular application to the use of ground wave radar in remote sensing of the marine environment.

Prof. Gill is a member of the American Geophysical Union.



Jochen Horstmann received the Diploma (Dipl.-Oz.) degree in physical oceanography and the Ph.D. (Dr.rer.nat.) degree in earth sciences from the University of Hamburg, Hamburg, Germany, in 1997 and 2002, respectively.

In 1995, he joined the GKSS Research Center (currently, Helmholtz-Zentrum Geesthacht Centre for Materials and Coastal Research), Geesthacht, Germany, where he has been a Research Scientist since 2002. In 2002, he was a Visiting Scientist with the Applied Physics Laboratory, John Hopkins University, Laurel, MD, USA, and also with the National Environmental Satellite, Data, and Information Service of NOAA, Washington, DC, USA. In 2004 and 2005, he was a Visiting Scientist with the Center for Southeastern Tropical Advanced Remote Sensing, University of Miami, FL, USA. Since 2007, he has been an Adjunct Professor with the Rosenstiel School of Marine and Atmospheric Science, University of Miami. From 2008 to 2013, he was a Senior Remote Sensing Scientist with the Center for Maritime Research and Experimentation of the NATO Science and Technology Organization in La Spezia, Italy. Since 2013, he has been the Head of the Department of Radar Hydrography with the Institute of Coastal Research, Helmholtz-Zentrum Geesthacht Centre for Materials and Coastal Research. He has a wide experience in the field of radar remote sensing, with respect to ocean wind, waves, and currents, and he has authored and coauthored more than 45 articles in international peer-reviewed journals. His main research interests include the development of oceanographic applications using radar-based sensors to investigate ocean-surface and near-surface processes.